Lecture 6: Internal tides

Myrl Hendershott and Chris Garrett

1 Introduction

So far, we have only considered barotropic tides, which have no vertical structure. In this lecture we turn our attention to baroclinic modes, which do have vertical structure. These are also referred to as *internal tides.*

Internal tides are internal waves forced by the interaction of the barotropic tides with the bottom topography of the oceans. To understand how internal tides can be generated in the ocean, it is useful to go through the properties of internal waves.

2 Internal waves

Internal waves in the ocean are the response of a rotating, density stratified, incompressible fluid to small perturbations. To derive the governing equations for these waves, we begin with the equations of motion for a fluid on a rotating Earth (see lecture 2), use the Boussinesq approximation and linearize about a base state of rest given by $\mathbf{u} = 0$, $\rho = \rho_0(z)$ and $p = p_0(z)$ where $\mathbf{u}$ is the velocity vector, p the pressure and ρ the density. Incompressibility is then

$$\frac{\partial u}{\partial x} + \frac{\partial v}{\partial y} + \frac{\partial w}{\partial z} = 0, \tag{1}$$

and the momentum equations become

$$\frac{\partial u}{\partial t} - fv = -\frac{1}{\rho_0}\frac{\partial p}{\partial x}, \tag{2}$$

$$\frac{\partial v}{\partial t} + fu = -\frac{1}{\rho_0}\frac{\partial p}{\partial y}, \tag{3}$$

$$\frac{\partial w}{\partial t} = -\frac{1}{\rho_0}\frac{\partial p}{\partial z} - \frac{\rho}{\rho_0}g, \tag{4}$$

where f is the Coriolis parameter and ρ and p are the perturbations to the density and pressure fields respectively. The continuity equation becomes

$$\frac{\partial \rho}{\partial t} + w\frac{\partial \rho_0}{\partial z} = 0. \tag{5}$$

And, from the momentum equations, it is also possible to find the energy equation

$$\frac{\partial}{\partial t}\left[\frac{1}{2}\rho_0(u^2 + v^2 + w^2)\right] + \nabla \cdot (p\mathbf{u}) = -w\rho g\hat{k}, \tag{6}$$

where $\hat{k}$ is the unit normal in the z-direction.

From (1)-(5), the equation for internal waves may be derived

$$\frac{\partial^2}{\partial t^2}\left[\nabla^2 w\right] + f^2\frac{\partial^2 w}{\partial z^2} + N^2\nabla_h^2 w = 0, \tag{7}$$

where $N = (-g/\rho_0\,\mathrm{d}\rho_0/\mathrm{d}z)^{-1/2}$ is the Brunt–Väisälä frequency, assumed constant for simplicity in this lecture unless otherwise stated. Subscript h refers to derivatives in the horizontal plane. We refer the reader to [1] for a derivation and we observe as a reminder that we are considering the situation where the hydrostatic approximation is not valid, since gravitational (or buoyancy) force is essential for the motion.

In the process of obtaining (7), the continuity equation (1) is used to substitute the vertical velocity for the horizontal velocities in the horizontal momentum equations (2) and (3). The result is an equation in w with a forcing term dependent on the horizontal variation of pressure

$$\frac{\partial^3 w}{\partial^2 t\,\partial z} + f^2\frac{\partial w}{\partial z} = \frac{\partial}{\partial t}\frac{\nabla_h^2 p}{\rho_0}. \tag{8}$$

If the disturbance is allowed no horizontal dependence, the above equation describes a harmonic oscillation with frequency f.

Another equation for w of second order in time can be obtained by differentiating in time the vertical momentum equation (4) giving

$$\frac{\partial^2 w}{\partial t^2} + N^2 w = -\frac{1}{\rho_0}\frac{\partial^2 p}{\partial t\,\partial z}. \tag{9}$$

Here a harmonic oscillation of frequency N is obtained if the perturbation has no vertical dependence.

The wave equation (7) is obtained by eliminating pressure between these two expressions, and the above remarks suggest that there will be two limiting cases for the motion. This also calls our attention to the fact that (7) has the structure of a double uncoupled harmonic oscillator. We anticipate that the frequencies of these wave motions will depend only on their angle with respect to the x-y plane and to the vertical direction and not on their amplitude. This 'azimuthal' angle determines how the horizontal and vertical forces at play combine to make the restoring force, while the amplitude has no effect on the frequency of a harmonic oscillator.

Equation (7) has an interesting spatial property, which can be better appreciated if we eliminate the temporal dependence by substituting $w = W(x, y, z)e^{-i\omega t}$ into (7). We obtain

$$W_{zz} - \left[\frac{N^2 - \omega^2}{\omega^2 - f^2}\right](W_{xx} + W_{yy}) = 0. \tag{10}$$

If the term in square brackets is positive, then the vertical and horizontal derivatives have different signs, which reflects the anisotropy in space introduced by the vertical stratification. Furthermore the equation is hyperbolic, which allows for energy propagation. If however the term is negative, then (10) is simply Laplace's equation, but for a scale transformation, and does not allow propagation of energy. This is another way of acknowledging the two limiting cases for the motion pointed out earlier: the equation allows for traveling waves with frequencies between f and N.

2.1 Internal wave solutions

We now consider solutions of (10) in an infinite fluid. The equation may be solved in two ways. Firstly, we may solve it assuming a plane wave form of solution and hence we substitute the trial solution

$$W = W_h e^{i(kx+ly+mz)} \tag{11}$$

into (10). This leads to the dispersion relation

$$\omega^2 = \frac{N^2(k^2+l^2)+f^2m^2}{k^2+l^2+m^2}. \tag{12}$$

Substituting the wave solution (11) into the continuity equation we get

$$\mathbf{k}\cdot\mathbf{u} = 0, \tag{13}$$

where $\mathbf{k}$ is the wave vector and $\mathbf{u}$ the velocity vector. That is to say, the wave vector is perpendicular to the displacement of the particles.

To simplify calculations from now on we assume, without loss of generality, that we have orientated the x-axis in the direction of the horizontal component of the wave vector. The dispersion relation (12) then becomes

$$\omega^2 = \frac{N^2k^2+f^2m^2}{k^2+m^2}, \tag{14}$$

and from it we can calculate the group velocity $\mathbf{c}_g = (c_{gx}, c_{gz})$

$$\mathbf{c}_g = \frac{\partial\omega}{\partial\mathbf{k}} = \ [N^2-f^2]\frac{mk}{\omega(k^2+m^2)^2}(m,-k), \tag{15}$$

and we observe that $\mathbf{k}\cdot\mathbf{c}_g = 0$. Hence the group velocity is also perpendicular to the wave vector. Furthermore we can see that the group velocity and wave vector always have opposite vertical components. This means that if phase propagates downwards energy propagates upwards and vice versa.

If we suppose that $\mathbf{x}(t) = (x(t), z(t))$ is the trajectory of the energy carried by the wave, then $\mathrm{d}\mathbf{x}/\mathrm{d}t = \mathbf{c}_g$ and so the trajectory is the curve that satisfies

$$\frac{dz}{dx} = \frac{c_{gz}}{c_{gx}} = -\frac{k}{m}. \tag{16}$$

This means that the energy trajectories are curves along which the independent variables are related by an ordinary differential equation. They are therefore also the characteristics of the wave equation.

Equation (10) may also be solved using characteristics. The solution, in two dimensions, is given by $W(x,z) = F(x+\alpha z) + G(x-\alpha z)$ where F and G are arbitrary functions and α is the ray slope, given by

$$\alpha^2 = \frac{N^2-\omega^2}{\omega^2-f^2}. \tag{17}$$

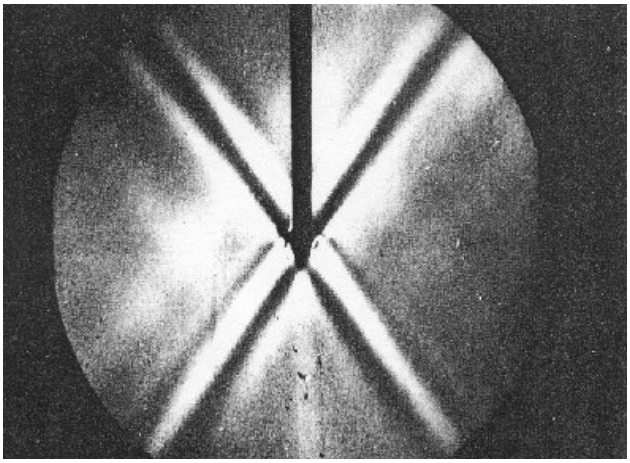

Figure 1: Schlieren image of internal waves, generated in a stratified fluid of constant N, by oscillation of a horizontal cylinder. Note that energy is propagating away along characteristics and surfaces of constant phase stretch out radially from the source. *From Mowbray and Rarity* [2].

If we substitute for ω from the dispersion relation (14) into the expression for α^2, then we find that it reduces to k^2/m^2 and so the result found through this procedure is equivalent to that found in the preceding paragraph.

The unusual properties of internal waves described in this section were observed experimentally by Mowbray and Rarity [2]. They placed an oscillating wave maker in a stratified fluid and observed the wave pattern shown in figure 1.

2.2 Internal waves in a finite depth of fluid

Equation (10) can also be solved for a rigid-lid upper surface and a planar bottom. A rigid-lid is an acceptable approximate boundary condition to use in place of a free surface, as it may be shown that internal waves only have a small surface displacement (see, for example, Pedlosky [1]). The solution is similar to (11), except that the vertical wavenumber is now quantized as

$$W = W_h e^{ikx - i\omega t} \sin\left(\frac{n\pi z}{H}\right), \tag{18}$$

in two dimensions, where H is the depth of the fluid.

This theory predicts the paths of propagation of energy for small perturbations in the ocean, and we see that it depends on the depth of the ocean and on the Brunt–Väisälä frequency. In this analysis, we have assumed that N is constant, however it can be shown (see, for example, Pedlosky [1]) that characteristics are also the ray paths for the WKB approximation for slowly varying N, the case for the ocean.

2.3 Interaction of internal waves with bottom topography

A final interesting property of internal waves is the way in which they interact with a sloping boundary. We refer the reader to Pedlosky [1] for a derivation of the reflection laws. Here we will limit ourselves to stating the results. Frequency is preserved by reflection, but not wavelength. If the slope of the boundary is less than that of the characteristics, the horizontal component of the wave vector is conserved under reflection. In other words, there is no back reflection from a boundary with slope inferior to that of the characteristics. Since all the energy is being transmitted forward, energy density must increase as the waves reach shallower water up the slope. If the slope goes all the way to the surface, energy density would be expected to be infinite at the apex. However, with each reflection the vertical wavenumber gets larger and the waves shorter. Group and phase velocities go rapidly to zero with the depth, so the wave never reaches the apex. In practice, as wavelengths become too small, the linearity assumption breaks and dissipative process come into play. Note also that the closer the slope of the surface is to that of the characteristics, the more intense the focusing effect, as can be seen in figure 2a.

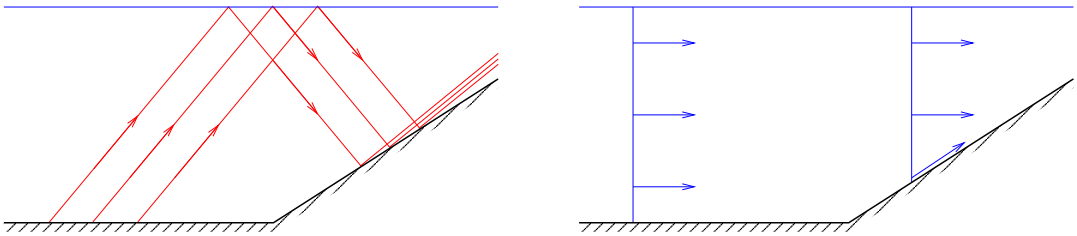

Figure 2: (a) Internal wave characteristics approaching a sloping boundary. After reflection, the energy in the waves is concentrated into a narrower band. If the boundary has slope equal to that of the characteristics, then all characteristics after reflection lie on the same line. (b) A barotropic velocity profile impinging on a sloping boundary. On the boundary, the velocity vector can only have a component tangential to it and hence over the slope, the velocity profile is no longer barotropic.

This behaviour of internal waves in interaction with a sloping boundary was observed in Sandstrom's [3] experiments: the amplification from a sloping bottom was clearly demonstrated.

3 Internal waves in the oceans

It is nowadays accepted that the interaction of the barotropic tide with bottom topography in the oceans is one source of internal waves, in this case the waves are referred to as internal tides. One way to conceptualize this generation is to imagine that, instead of a tidally oscillating ocean with a fixed bottom, the water of the ocean is fixed and the bottom oscillates with tidal frequency. The oscillations of topography then behave as oscillating wave makers, as in the experiment of Mowbray and Rarity described in §§2.1.

However, in the past, the curious behaviour found for the solutions of (7) led to doubts about whether it was in fact a suitable equation to describe the response of the oceans to small perturbations. Another question of interest was whether these waves could be generated in the ocean by the barotropic tides. It was imagined that a sloped boundary could act as a source of internal waves, in the case of a barotropic impinging disturbance. As illustrated in figure 2b, a barotropic disturbance cannot meet the zero normal component requirement at the slope and remain barotropic. Its energy must go into generating internal waves, and propagate away along characteristics. These two questions motivated a number of numerical and observational efforts, some of which we will briefly be described below.

Figure 3 shows the result of a numerical calculation where a barotropic tide was made to impinge on a step-like slope. No specific mode structure can be recognized in the reflected perturbation, because a composition of many is necessary to conform to such an abrupt boundary. However, the results clearly show that the reflected perturbation is baroclinic and propagates along the characteristics.

Regal and Wunsch [5] attempted an observational verification of propagation of energy along characteristics for a real slope, shown in figure 4a, with the measured profile of N shown in figure 4b. They found that the shape of the boundary coincided with that of the characteristics. This meant that intense focusing of energy would occur along the slope. After bottom reflection, this energy would travel to point D on the surface. An energy profile below point D does in fact show concentration near the surface.

Even once it was reasonably established that internal waves can be generated by the interaction of the barotropic tides with topographic features, it remained to be clarified whether these motions had only local influence over ocean dynamics or if they could propagate away for large distances and be ubiquitous in the ocean. This question was addressed using data of an experiment originally designed to study mesoscale circulation in the ocean.

The Mid-Ocean Dynamics Experiment (MODE) provided data that proved very useful for the study of internal waves. The setup consisted of a two dimensional array of current, temperature and pressure profiling moorings as shown in figure 5a. These were arranged in three concentric circles with radii 50, 100 and 180 km, situated over a smooth abyssal plane of depth 5400 km. Being 700 km away from the nearest large topographic feature, this array was far from any source of internal tides. If significant signals of internal waves were detected, then they would have traveled far to get there.

The two dimensional arrangement of moorings could be used as an antenna, the difference in arrival times of a given phase surface in different moorings could be used to infer the direction of propagation of the signal. Internal waves with M_2 and S_2 frequencies were detected coming from the general direction of the nearest major topographic feature, 700 km away. The period and direction of incidence of these signals were strong indications that they were in fact internal tides generated at the Blake Escarpment. Averages over the whole data collecting period for each mooring showed very significant baroclinic contribution to their structure in some cases, indicating that the internal waves were an important part of the local dynamics, as shown in figure 5b.

These results showed that internal tides, once generated, could travel large distances and have a significant influence over the dynamics of the open ocean. They also suggested that a significant portion of the barotropic tidal energy was going into baroclinic tides, since baroclinic and barotropic contributions seemed to have comparable amplitudes in some of

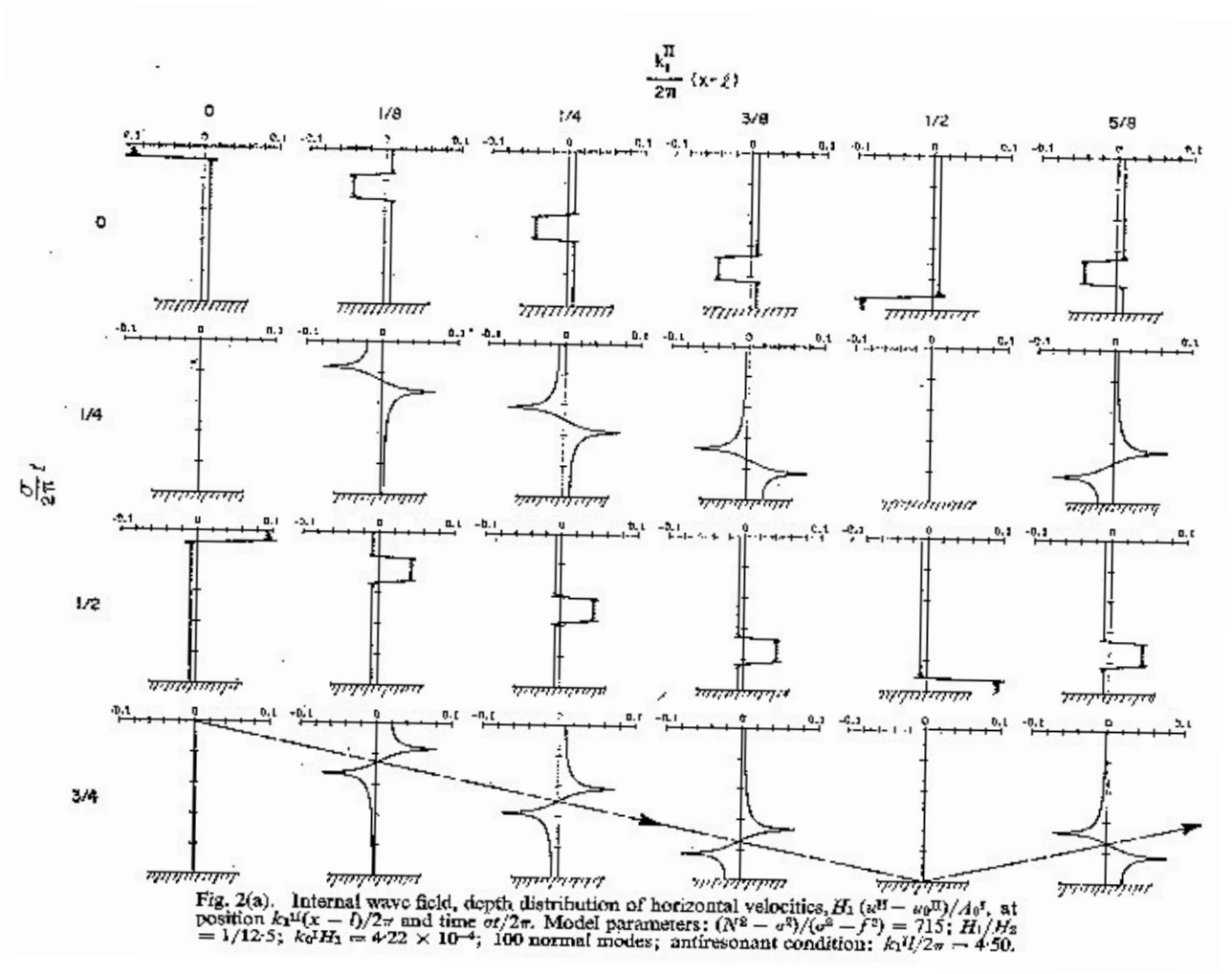

Fig. 2(a). Internal wave field, depth distribution of horizontal velocities, H_1 $(\kappa^{II} - \omega_0^{II})/A_0^I$, at position $k_1^{II}(x - l)/2\pi$ and time $\sigma t/2\pi$. Model parameters: $(N^2 - \sigma^2)/(\sigma^2 - f^2) = 715$; $H_1/H_2 = 1/12{\cdot}5$; $k_0^I H_1 = 4{\cdot}22 \times 10^{-4}$; 100 normal modes; antiresonant condition: $k_1^{II} l/2\pi = 4{\cdot}50$.

Figure 3: Depth distribution of horizontal internal tidal currents at increasing distances away from a step shelf (top) at two times (centre and bottom) separated by a quarter-wave period. The profile is seen to follow the rays (arrows in bottom) away from the slope. *From Rattray et al.* [4].

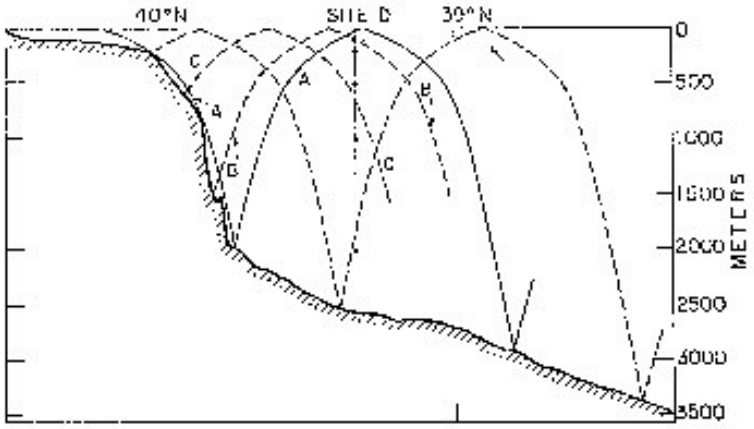

Fig. 4. The topography of the continental margin to the north of Site D, indicating the two families of characteristics originating along the continental slope and passing through the mooring. Notice that one characteristic, marked 'A', is virtually tangent to the slope and eventually reaches the surface near Site D. Characteristics shown as dashed, two of which are marked 'B' and 'C', also tend to focus near the surface (adapted from FOFONOFF, 1966).

(a)

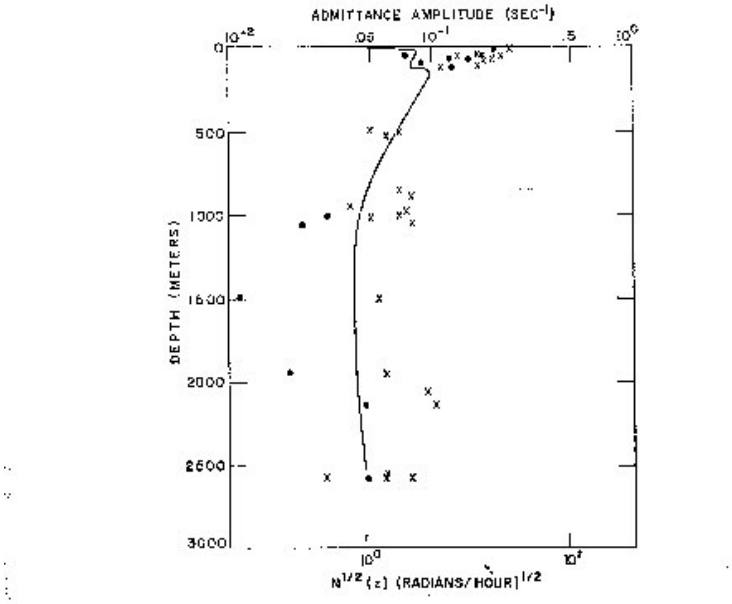

Fig. 2. Admittance amplitudes U and V as a function of depth at Site D. The curve indicates the average square root buoyancy frequency at this location. Though the position of this $N^{1/2}(z)$ curve is arbitrary, we have chosen it to pass through the bulk of the points, clearly showing the near surface intensification. (Cross is U, dot is V.)

(b)

Figure 4: (a) Profile of relief along 70° W together with selected semi-diurnal characteristics passing near site D. (b) Admittance amplitude × for semi-diurnal tidal currents together with Brunt–Väisälä frequency $N(z)$, solid line, at site D. Near surface admittances are strongly intensified. *From Regal and Wunsch* [5].

the mooring averages.

Probably the main reason why the role of baroclinic tides in ocean dynamics was only recently fully acknowledged is their small effect on surface elevation. Typically of only a few centimetres, surface elevation due to internal tides was historically dismissed as noise in satellite data. However the shortcomings in the attempts to infer underwater currents from surface displacement, illustrated in figure 6 are evidence of their role.

Surprisingly it is the small effect on surface elevation that has recently made global coverage possible in internal tide observation, because these small displacements have been successfully observed by satellites, as shown in figure 7.

4 Mixing and internal tides

Internal tides are currently receiving renewed attention due to their role in ocean mixing. In the absence of mixing, the temperature and salinity profiles of the ocean would be uniform, barring a thin surface layer heated by the Sun. Cold, dense water generated at the poles would sink and flow equatorward and upwell. Eventually, water of this property would fill the oceans up to the depth at which solar radiation penetrates. However, the real ocean does not have this structure, as shown in figure 8: vertical mixing prevents its realization.

Internal tides are one possible source of mixing. Two studies whose results support this statement were carried out in the Brazil Basin and the Monterey Canyon off the coast of California. Figure 9a shows levels of turbulent diffusivity across the Brazil Basin. Enhanced diffusivity, and hence mixing, is seen over the rough topography compared to over the smooth topography. This suggests the involvement of bottom topography in ocean mixing, at least at abyssal depths. Both tidal flow, and mean or eddy flows, over topography generate internal waves. However, in this data, a modulation of the dissipation rate over the spring-neap cycle suggests the waves are internal tides.

Figure 9b shows levels of turbulent dissipation along a section extending off the slope of the continental shelf. Enhanced levels are seen along the ray path of a semi-diurnal tide beam, out to more than 4 km away from the topography. Where internal waves dissipate and cause mixing is not really known. It is thought that non-linear wave-wave interactions and scattering when internal waves reflect off the ocean floor cause low vertical wavenumber modes to cascade to higher wavenumbers. At higher vertical wavenumbers, there is increased vertical shear and eventually a shear instability, and hence mixing, results.

However, low wavenumber modes are relatively stable to wave-wave interactions. In scattering also, much of the low modes are preserved and so low modes tend to survive many bottom encounters. This results in a general persistence of low mode internal tides, and they have been observed to propagate to $O(1000\,\mathrm{km})$ from their source, as described in §3.

5 Conversion of energy from barotropic to internal tides

As a first step towards understanding the contribution of internal tides to ocean mixing, research has been conducted into finding the amount of energy converted from barotropic

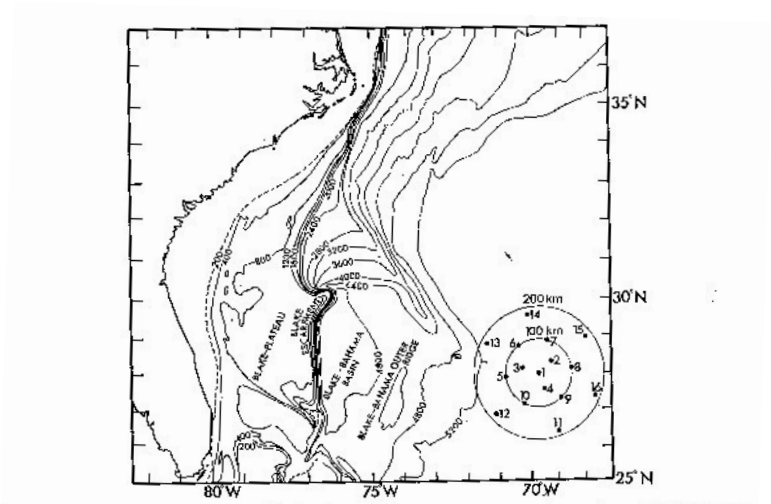

FIGURE 1. Chart of the MODE area, showing the array of fixed moorings. Bathymetric contours in metres.

(a)

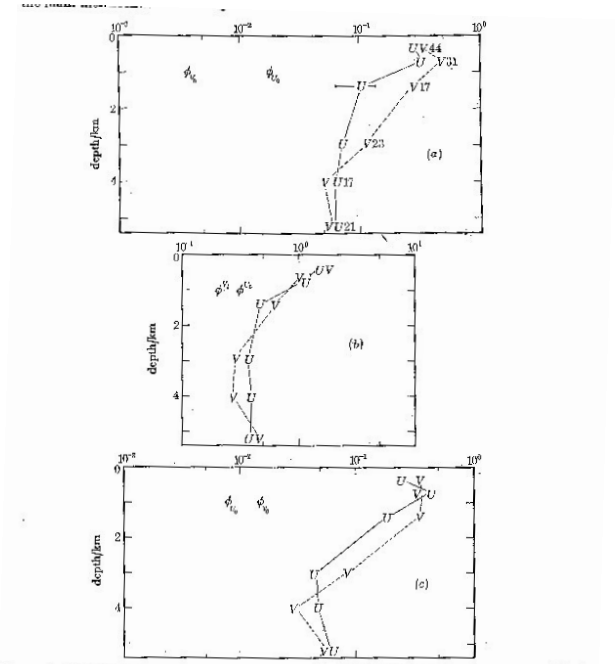

FIGURE 3a. Vertical profile of squared horizontal current ((cm/s)²) for U (east) and V (north) in the S_2 band, averaged at depth levels over the entire array. Estimates of squared amplitude for the barotropic current components U_0 and V_0 are given, showing that the currents are dominated by internal waves at all depths.

FIGURE 3b. Similar estimates for the M_2 band currents. Here the deep currents are greatly influenced by the barotropic mode.

FIGURE 3c. Similar estimates for the N_2 band. Internal waves appear to dominate at all depths.

(b)

Figure 5: (a) Chart of the MODE area, showing the array of fixed moorings. Bathymetric contours are in metres. (b) Vertical profile of the squared horizontal current ($\mathrm{cm^2 s^{-2}}$) for U (east) and V (north) in the (a) S_2 and (b) M_2 band, average at depth levels over the entire array. Estimates for the squared amplitude for the barotropic current components U_0 and V_0 are also given. For the S_2 band, the current is seen to be dominated by internal waves at all depths. For the M_2 band, the deep currents are greatly influenced by the barotropic mode. *From Hendry* [6].

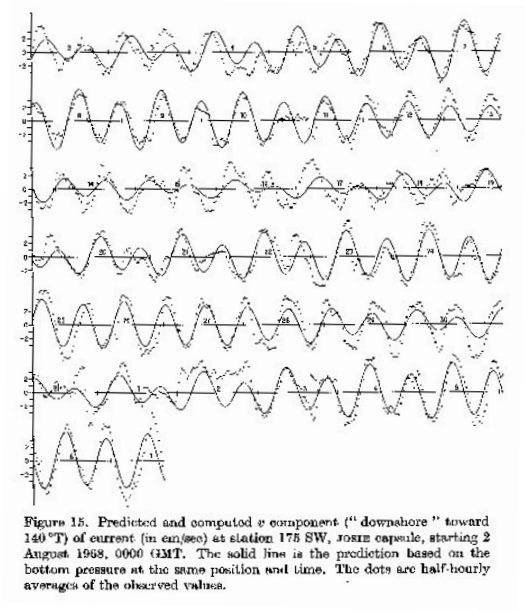

Figure 15. Predicted and computed v component ("downshore" toward 140 °T) of current (in cm/sec) at station 175 SW, JOSIE capsule, starting 2 August 1968, 0000 GMT. The solid line is the prediction based on the bottom pressure at the same position and time. The dots are half-hourly averages of the observed values.

Figure 6: Observed (dotted) and predicted barotropic (solid) longshore bottom velocity off the southern California coast. *From Munk et al.* [7]

.

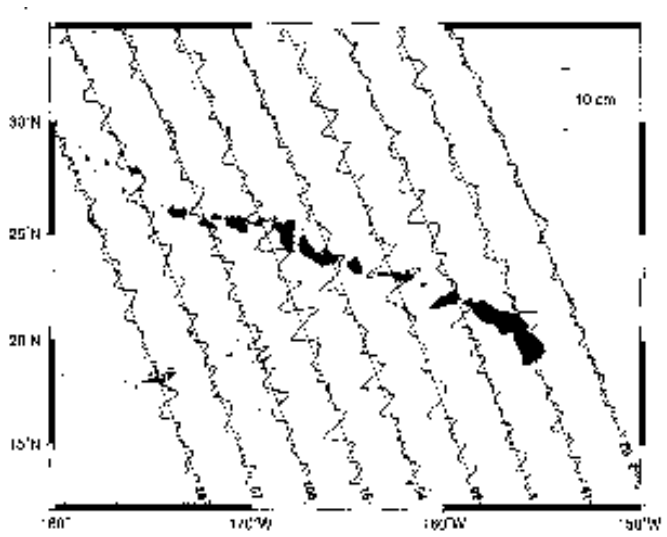

Figure 7: High-pass filtered estimates of M_2 tidal amplitudes plotted along Topex–Poseidon ground tracks. Background shading corresponds to bathymetry, with darker denoting shallower water. *From Ray and Mitchum* [8]

.

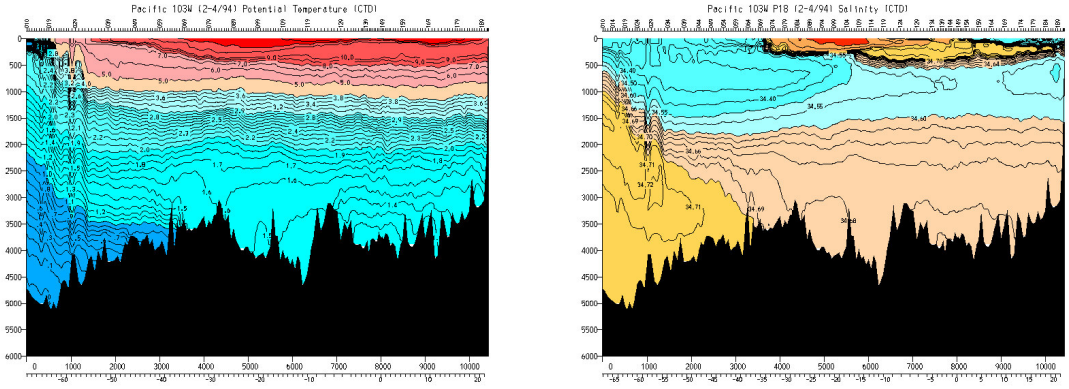

(a) (b)

Figure 8: (a) Potential temperature and (b) salinity profiles along a section of the Pacific Ocean from approximately 70° S to 20° N. Red indicates high values and blue low. The high salinity values at the surface are due to evaporation. *From the World Ocean Circulation Experiment.*

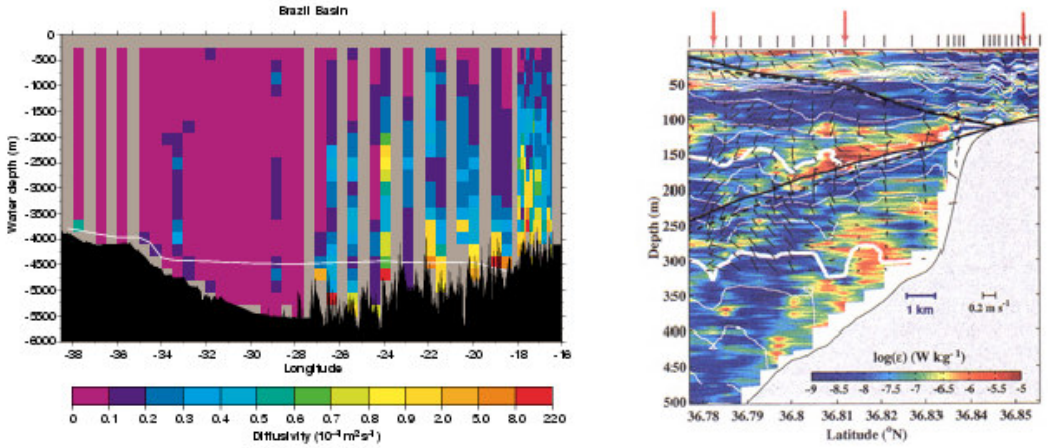

(a) (b)

Figure 9: (a) A section of turbulent diffusivity across the Brazil Basin. The bottom bathymetry is shown from a representative transect with the apex of the Mid-Atlantic Ridge at 12° W. *From Toole et al.* [9]. (b) A section of turbulent dissipation rate ϵ off the shelf break slope in Monterey Bay, California. The solid black lines are the ray paths of semi-diurnal tide beams. *From Lien and Gregg* [10].

to baroclinic tides. As discussed in §3, the interaction of the barotropic tide with bottom topography in the oceans results in the generation of internal tides.

Cox and Sandstrom [11] and Bell [12] developed linear[1] theories to model the generation of internal tides from the barotropic tide. Rough estimates originally suggested that the energy flux from barotropic to internal tides (contributing to energy loss in the deep oceans) was much less than the energy dissipated in shallow seas, as shown in figure 10. However, even if only 10% of the total energy loss of the barotropic tides took place in the deep oceans, it would contribute significantly to abyssal mixing.

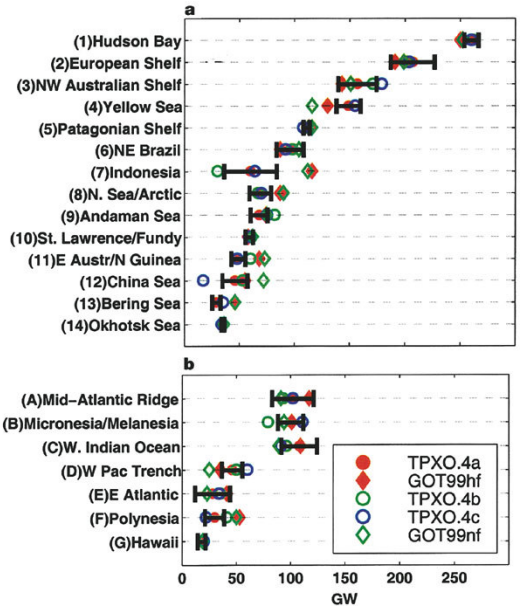

Figure 10: Area-integrated dissipation for various shallow seas and deep-ocean areas. *From Egbert and Ray* [13]

.

Egbert and Ray [13, 14] examined least-squares fits of Topex–Poseidon altimetry data to models for the global barotropic tide. They interpreted model residuals in terms of 'tidal dissipation' with this referring to any mechanism that transfers energy out of the barotropic tides: they were not able to distinguish whether barotropic energy is lost to baroclinic modes or to bottom friction. Figure 11 shows the regions of significant 'tidal dissipation'.

About 0.7 TW of power is lost from M_2 barotropic tides in the deep ocean. The fraction of this associated with frictional dissipation can be estimated from the drag force $\rho c_D |u| u$ where $c_D = 0.0025$ is the drag coefficient. For typical open ocean tidal speeds of $u \simeq 0.03\,\mathrm{ms}^{-1}$, the frictional dissipation is less than $0.1\,\mathrm{mWm}^{-2}$, or less than 30 GW globally. Thus nearly all barotropic tidal loss in the deep ocean must occur as internal tide generation.

One possible location for significant internal tide generation is at continental slopes. In some places, such as the north-western Australian shelf and the Bay of Biscay, generation

[1]Linear will be defined more precisely in §§5.1. Essentially, it assumes that the heights and slopes of topographic features are small.

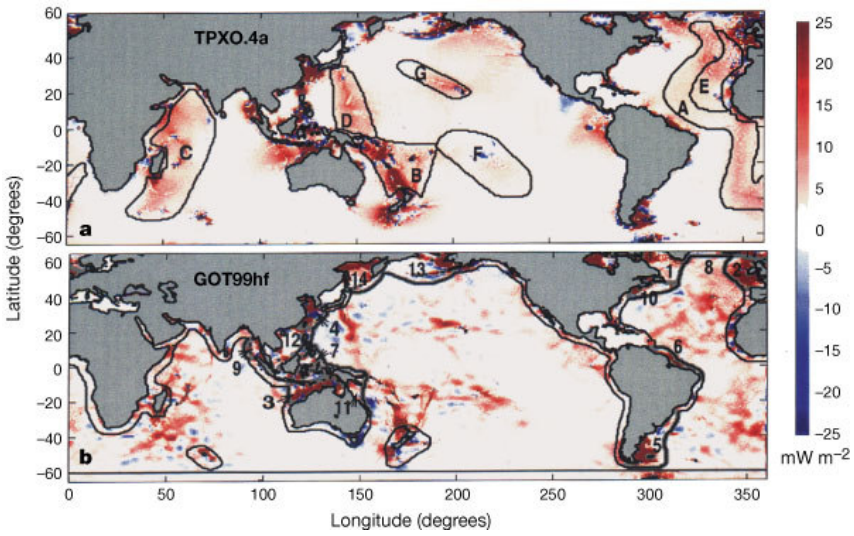

Figure 11: Global distribution of barotropic energy loss. The estimates were made using observations of sea surface elevation from the Topex–Poseidon altimeter. Positive values (red) show energy loss. Negative values (blue) indicate regions where noise prevented accurate estimates. *From Egbert and Ray* [14].

at the continental shelf is significant because the tidal flow is perpendicular to the shelf, as in figure 12a. However, in many places tidal flow is parallel to the coast, as in figure 12b and hence internal tide generation is small. For a few decades, this area was the main focus of research into internal tides.

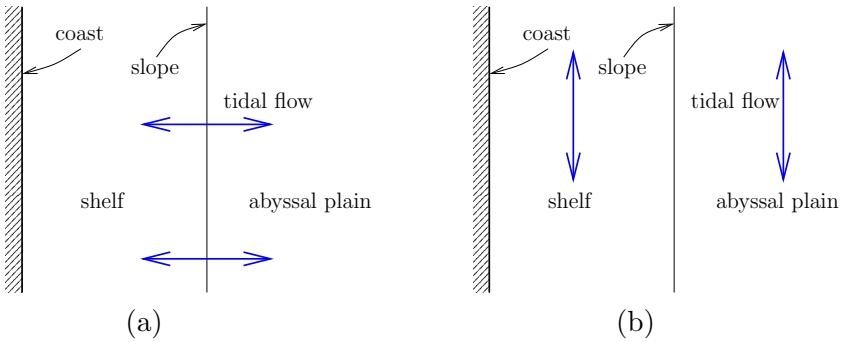

Figure 12: The approximate flow of the barotropic tide close across the continental shelf. (a) Flow perpendicular to the slope and (b) flow parallel to the slope.

The other main possibility for significant internal tide generation is at mid-ocean ridges and ocean island chains such as the Hawaiian Ridge. Recently, research has focused on this aspect of internal tide generation. Following this work, we calculate the energy conversion between the barotropic tide and the internal tides for different topographies. For this, we consider two approaches: linear theory for small slope, small height topography and a full

theory for infinitely steep topography. In both approaches, the Brunt-Väisälä frequency is assumed constant and we restrict ourselves to two-dimensional problems.

5.1 Linear theory for energy conversion

Consider a barotropic tide $U_0 \cos \omega t$, where ω is an astronomically determined forcing frequency (for example the frequency of the M_2 or S_2 tide), over rough topography as shown in figure 13.

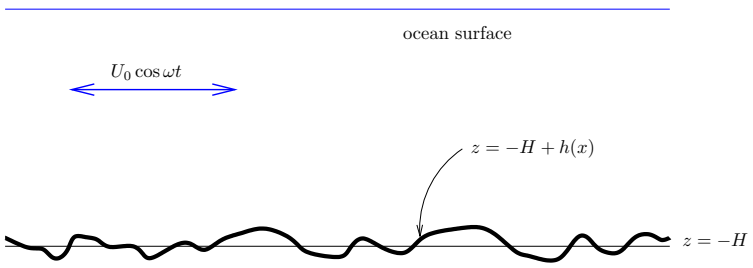

Figure 13: A barotropic tide $U_0 \cos \omega t$ across a rough bottom $z = -H + h(x)$ where $h(x)$ is a bottom topography relative to a deep constant depth level $z = -H$.

We first look at the three key dimensionless parameters of the problem.

- $\frac{\text{tidal excursion}}{\text{horizontal scale of topography}} = \frac{U_0 k}{\omega}$ where k is a wavenumber associated with the horizontal scale of the topography;
- $\epsilon = \frac{\text{maximum bottom slope}}{\text{slope of characteristics}}$ with $\epsilon < 1$ referred to as *subcritical* as the rays have steeper slope than the bottom topography, $\epsilon = 1$ is *critical* and $\epsilon > 1$ is *supercritical*;
- $\delta = \frac{\text{maximum topographic height}}{\text{ocean depth}} = \frac{h_0}{H}$ where h_0 is an amplitude associated with the bottom topography and H is the depth of the ocean.

In addition there are two dimensionless numbers ω/f and ω/N which specify the time-scale of the tide relative to the inertial and buoyancy time scales.

5.1.1 Assumptions

Firstly, it is assumed that the tidal excursion is much smaller than the horizontal scale of the bottom topography. If this were not the case, then the topography would essentially see a nearly constant current across it, although switching direction over the tidal cycle. Quasi-steady lee waves would then form on the downstream side of the topography. For M_2, and with deep ocean currents of the order $10^{-2}\,\mathrm{ms}^{-1}$, the tidal excursion is of the order of 100 m and so $U_0 k/\omega$ is indeed small.

Secondly, the linear theory requires that ϵ and δ are also small. Note that as the wavenumber k associated with the bottom topography gets higher, ϵ increases since the characteristic slope, α from (17) is fixed by fixing ω but the slope of the topography is proportional to k. Hence, for sufficiently high wavenumbers, the linear theory will always get into trouble. From observations by St. Laurent and Garrett [15], over 90% of the energy flux is accounted for in wavenumbers below critical at mid-ocean ridges.

5.1.2 Energy flux

At the bottom, the boundary condition of zero normal flow, in linearized form, becomes

$$w|_{z=-H} = U_0 \frac{\mathrm{d}h}{\mathrm{d}x},$$

where w is the vertical component of the baroclinic wave response, and so $w \propto k$. From the dispersion relation for internal waves (14), it can be seen that the vertical component of the group velocity for a rigid-lid solution (18) is

$$c_{gz} = \frac{\partial \omega}{\partial (n\pi/H)} = -\sqrt{\frac{(\omega^2 - f^2)^3 (N^2 - \omega^2)}{\omega^2 (N^2 - f^2)^2}} k^{-1},$$

and so $c_{gz} \propto k^{-1}$ since ω is a fixed forcing frequency.

Hence the kinetic energy is proportional to k^2 and the vertical energy flux to internal tides has the form

$$F_{\text{linear}} \propto c_{gz} \times w^2 \propto k \times \text{bottom topography spectrum},$$

where the subscript 'linear' implies we are considering the linear regime. We can use Fourier decomposition and superposition to obtain solutions for arbitrary topography.

Llewellyn Smith and Young [16] showed that the horizontal energy flux away from the topography is in fact

$$F_{\text{linear}} = F_0 \alpha \pi H^{-3} \sum_{n=1}^{\infty} k_n \tilde{h}(k_n) \tilde{h}^*(k_n), \tag{19}$$

where the Fourier transform is defined as

$$\tilde{h}(k_n) = \int_{-\infty}^{\infty} h(x) e^{-ikx} \mathrm{d}x,$$

and the modes are given by $k_n = \alpha \pi n / H$, from (14), where α is the ray slope given in (17) and

$$F_0 = \frac{1}{2\pi} \rho_0 \omega^{-1} \sqrt{(N^2 - \omega^2)(\omega^2 - f^2)} U_0^2 H^2.$$

We now consider two different forms for the topography and calculate the associated energy fluxes.

5.1.3 A small, subcritical ridge

Assume a bottom topography given by a Witch of Agnesi curve[2]

$$h(x) = h_0 \left(1 + \frac{x^2}{b^2}\right)^{-1},$$

as shown in figure 14a. Here b parameterizes the width of the topography.

[2]Originally this curve was given the Latin name *versoria* which means 'rope that turns a sail' from the construction resulting in this curve. This became the Italian *la versiera*, but on translation into English, of a textbook by Maria Agnesi, it was mistaken for *l'aversiera*, or 'witch'.

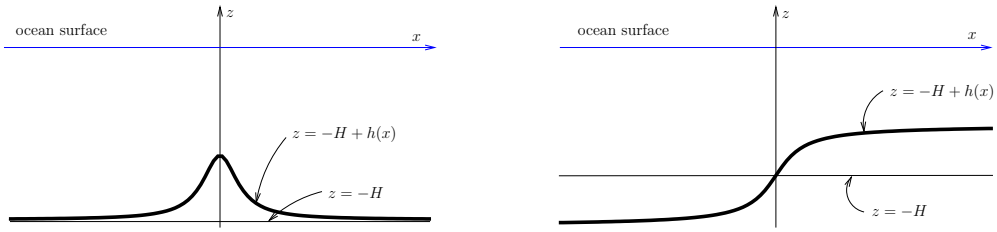

Figure 14: The profiles for (a) a small, subcritical ridge and (b) a small, subcritical step.

Provided that $\delta \ll 1$ and the maximum slope of the Witch, $(3^{3/2}/8)(h_0/b)$, is sufficiently small so that $\epsilon \ll 1$, the problem is linear. The Fourier transform of the Witch is $\tilde{h}(k) = bh_0\pi e^{-kb}$ and hence

$$F_{\text{linear}} = F_0 \frac{\pi^2}{4}\delta^2 \sum_{n=1}^{\infty} nc^2 e^{-nc},$$

where $c = (3^{3/2}\pi/4)(\delta/\epsilon)$ and $\epsilon = \alpha^{-1}(3^{3/2}/8)(h_0/b)$. Hence we have an expression for the energy loss to internal tides.

One further question which may be asked is how strongly the result depends on the width of the topographic feature. In the small δ/ϵ limit $F_{\text{linear}} \sim F_0\pi^2\delta^2/4$, hence in the deep ocean the flux is independent of the ridge width.

This type of profile is appropriate for mid-ocean ridges which have subcritical slopes and are relatively small compared with the overall depth of the ocean.

5.1.4 A small, subcritical step

The bottom topography is given by

$$h(x) = \pi^{-1}h_0 \tan^{-1}\frac{x}{b},$$

as shown in figure 14b. It should be noted that the derivative is proportional to the Witch profile and, using this fact and integration by parts, the Fourier transform becomes $\tilde{h}(k) = -ih_0k^{-1}e^{-kb}$. The flux is now

$$F_{\text{linear}} = F_0\delta^2 \sum_{n=1}^{\infty} n^{-1}e^{-2n\delta/\epsilon},$$

where $\epsilon = h_0/(b\pi\alpha)$.

For small δ/ϵ, we obtain

$$F_{\text{linear}} \sim F_0\delta^2 \log(\epsilon/2\delta). \tag{20}$$

Hence, unlike the ridge in §§5.1.3, the flux remains dependent on the width of the sloping region, even in a deep ocean.

It should be noted, that it is not possible to approximate arbitrary topography by a series of independent steps, as was done by Sjöberg and Stigebrandt [17]. The flux at each

step, if isolated and independent, is proportional to $\delta^2 \log \delta$ as this will be shown later to apply even for an abrupt step. If there are n steps, then $\delta \propto h_0/n$ and the total energy flux is $F_{\text{linear}} \propto n \times h_0^2 n^{-2} \log n$, which tends to 0 as n tends to infinity.

5.2 Energy conversion at supercritical topography

For supercritical topography, $\epsilon > 1$ and the linear theory of the previous section is no longer valid. In this case, it is possible to use a Fourier series decomposition and matching to study some limiting cases: a knife-edge ridge and a Heaviside step.

5.2.1 A knife-edge ridge

The topography in this case is assumed to consist of a knife-edge of height h_0, as shown in figure 15a.

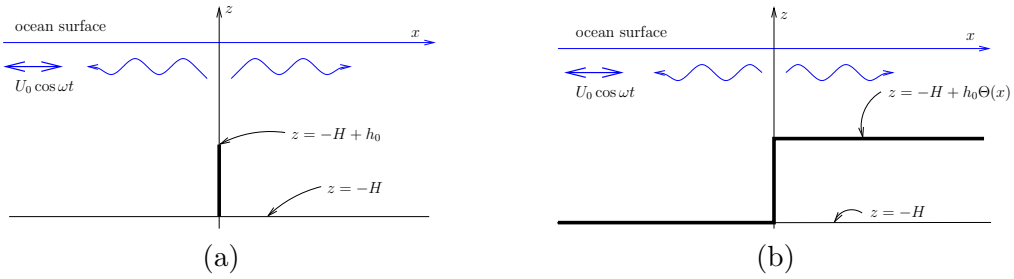

Figure 15: The profiles for (a) a knife-edge ridge and (b) a Heaviside step.

Note that the ratio of the tidal excursion to the horizontal scale of the topography will now necessarily be infinite, and quasi-steady lee waves should be expected. However we ignore these as the same analysis with a top-hat ridge gives very similar results (see St. Laurent *et al.* [18]).

The barotropic tidal current is given by $U_0 \cos \omega t$, perpendicular to the ridge. When incident on the knife-edge, it produces waves propagating to the left and to the right, at the same frequency as the barotropic tide. The form for the velocities in the reflected baroclinic modes are taken as

$$u_1 = U_0 \sum_{n=1}^{\infty} a_n \cos\left(\frac{n\pi z}{H}\right) \cos(k_n x + \omega t), \quad w_1 = \alpha U_0 \sum_{n=1}^{\infty} a_n \sin\left(\frac{n\pi z}{H}\right) \sin(k_n x + \omega t) \quad (21)$$

to the left of the knife and

$$u_2 = U_0 \sum_{n=1}^{\infty} b_n \cos\left(\frac{n\pi z}{H}\right) \cos(-k_n x + \omega t), \quad w_2 = -\alpha U_0 \sum_{n=1}^{\infty} b_n \sin\left(\frac{n\pi z}{H}\right) \sin(-k_n x + \omega t) \quad (22)$$

to the right, where α is the characteristic slope from (17). The form for w_i is assumed from (18) and the form for u_i follows from continuity equation (1). The form for the pressures may be derived using (21) and (22) and the linearized momentum equations (2) and (4) with $f = 0$.

There are matching conditions at $x = 0$ given by

$$w_1 = w_2, \qquad -H + h_0 \le z \le 0, \tag{23}$$

$$u_1 + U_0 = u_2 + U_0, \qquad -H + h_0 \le z \le 0, \tag{24}$$

$$u_1 + U_0 = 0, \qquad -H \le z \le -H + h_0, \tag{25}$$

$$u_2 + U_0 = 0, \qquad -H \le z \le -H + h_0. \tag{26}$$

The latter three conditions combine to give

$$\sum_{n=1}^{\infty} a_n \cos\left(\frac{n\pi z}{H}\right) = \sum_{n=1}^{\infty} b_n \cos\left(\frac{n\pi z}{H}\right), \qquad -H \le z \le 0,$$

which implies, from orthogonality of cosines, that $a_n = b_n$.

The remaining conditions then become

$$\sum_{n=1}^{\infty} a_n \sin\left(\frac{n\pi z}{H}\right) = 0, \qquad -H + h_0 \le z \le 0,$$

from (23) and

$$\sum_{n=1}^{\infty} a_n \cos\left(\frac{n\pi z}{H}\right) = -1, \qquad -H \le z \le -H + h_0,$$

from (25) or (26).

Multiplying by $\cos(m\pi z/H)$ and integrating vertically gives

$$\sum_{n=1}^{\infty} \left(\int_{-H}^{-H+h_0} \cos\left(\frac{n\pi z}{H}\right) \cos\left(\frac{m\pi z}{H}\right) \mathrm{d}z + \int_{-H+h_0}^{0} \sin\left(\frac{n\pi z}{H}\right) \cos\left(\frac{m\pi z}{H}\right) \right) \mathrm{d}z = - \int_{-H+h_0}^{0} \cos\left(\frac{m\pi z}{H}\right) \mathrm{d}z.$$

Curtailing the summation at M and taking $m = 0, 1, 2, \ldots, M-1$ gives a matrix equation to solve for a_n of the form $\mathsf{A}_{mn} a_n = c_m$ which may be solved numerically.

The flux of energy into the baroclinic modes may now be calculated. The conversion rate is equal to the energy flux away from the topography. From (6), this may be written as

$$F_{\text{knife}} = \int_{-H}^{0} < pu > \, \mathrm{d}z,$$

where $< \cdot >$ is the average in time. Hence $F_{\text{knife}} = F_0 \sum_{n=1}^{\infty} n a_n^2$.This flux is appropriate for calculating the flux from ocean island chains, such as Hawaii, since slopes at such features are supercritical.

The linear theory for a Witch profile gives a flux that is half that of a knife-edge in the deep ocean case, as shown in figure 16a (see St. Laurent *et al.* [18] and Llewellyn Smith and Young [19]). Various authors (see, for example, Balmforth *et al.* [20] and Pétrélis *et al.* [21]) have also considered the energy flux for other topographies and different values of the slope parameter ϵ. They find results that do not differ significantly when taking different

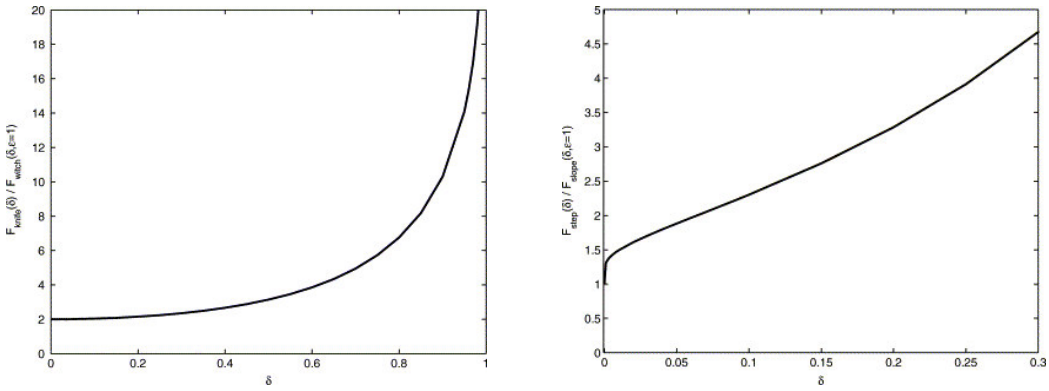

(a) (b)

Figure 16: The energy flux ratio for (a) the knife compared to the Witch and (b) the steep step compared to the inverse tan with $\epsilon = 1$ against δ. *From St. Laurent et al.* [18].

values of ϵ. The importance of this is that, in the deep ocean case, the slope (and hence the precise shape) of the topography is not the significant factor: the depth of the topography is the more important parameter.

It is also possible to use a similar technique to that given above to consider flow over a top hat ridge. Figure 17a shows the horizontal velocity profile for a steep step, similar to that for a top hat ridge, and figure 17b compares the energy flux from the top hat ridge to that from the knife edge.

5.2.2 A steep step

This is the extension of §§5.1.4 to an infinitely steep slope and is shown in figure 15b. We use the same procedure as in the previous subsection, however some modifications are required. The lack of symmetry across $x = 0$ implies that the wavenumbers to the left and right are not the same, and also $a_n \neq b_n$. Hence we set

$$u_1 = U_0 \sum_{n=1}^{\infty} a_n \cos\left(\frac{n\pi z}{H}\right) \cos(k_n x + \omega t), \quad w_1 = \alpha U_0 \sum_{n=1}^{\infty} a_n \sin\left(\frac{n\pi z}{H}\right) \sin(k_n x + \omega t) \quad (27)$$

on the deep side and

$$u_2 = U_0 \sum_{n=1}^{\infty} b_n \cos\left(\frac{n\pi z}{H - h_0}\right) \cos(-k_n' x + \omega t),$$
$$w_2 = -\alpha U_0 \sum_{n=1}^{\infty} b_n \sin\left(\frac{n\pi z}{H - h_0}\right) \sin(-k_n' x + \omega t) \quad (28)$$

on the shallow side.

The boundary conditions are similar to (23)-(26). Noting that the barotropic tide, by continuity, must scale by $H/(H - h_0)$ to the right of the step, the boundary conditions

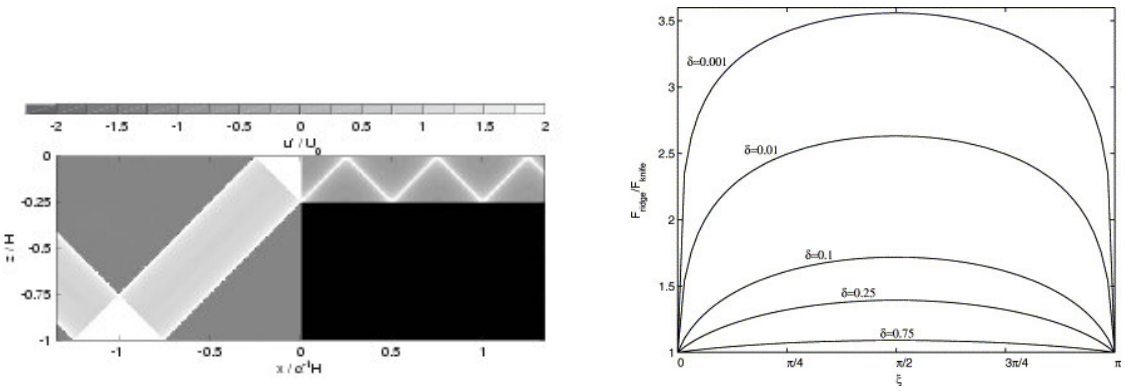

(a) (b)

Figure 17: (a) The baroclinic horizontal velocity profile resulting from a barotropic tide impinging on a steep step profile (the black rectangle). This profile is very similar to part of the profile seen for a top hat ridge. (b) Comparison between the energy flux of a top hat ridge with that of a knife edge. The fact that the curves become identical at $\alpha\pi L/H = \pi$, where L is the width of the ridge, is because the characteristic manages to fit into the ridge perfectly at this length. The worse agreement as δ become small is because the topography profile begins to look increasingly like two separate steps. *From St. Laurent et al.* [18].

become

$$\sum_{n=1}^{\infty} a_n \sin\left(\frac{n\pi z}{H}\right) = -\sum_{n=1}^{\infty} b_n \sin\left(\frac{n\pi z}{H-h_0}\right), \qquad -H+h_0 \le z \le 0, \quad (29)$$

$$1+\sum_{n=1}^{\infty} a_n \cos\left(\frac{n\pi z}{H}\right) = \frac{H}{H-h_0} + \sum_{n=1}^{\infty} b_n \cos\left(\frac{n\pi z}{H-h_0}\right), \qquad -H+h_0 \le z \le 0, \quad (30)$$

$$1+\sum_{n=1}^{\infty} a_n \cos\left(\frac{n\pi z}{H}\right) = 0, \qquad -H \le z \le -H+h_0. \quad (31)$$

Multiplying (30) and (31) by $\cos(n\pi z/H)$ and (29) by $\sin[n\pi z/(H-h_0)]$ and integrating the equations vertically gives a matrix equation to solve for a_n and b_n of the form

$$a_m = \mathsf{A}_{mn} b_n + C_m, \qquad b_n = \mathsf{B}_{nl} a_l,$$

which may be solved numerically. Again, the flux may be found, and comparing it to the flux from the slope profile in §§5.1.4, we see, as for the ridge/knife edge comparison, that the difference is relatively small between supercritical and critical slope topography (see figure 16b).

Overall the conclusion is that, in the deep ocean, increasing the steepness of topographic features beyond the critical slope of the internal tide rays does not lead to a dramatic increase in energy flux into internal tides. However, increasing the height of the features, relative to the ocean depth, leads to a greater than quadratic increase in flux.

6 Open questions

There are many possible directions for research in internal tides:

1. Theoretical and numerical models for three-dimensional obstacle of finite slope and height.
2. The fate of low mode internal tides generated at bottom topography. Do they
   (a) Break down in the ocean interior?
   (b) Cascade to higher modes and turbulence on re-encounter with the sea floor?
   (c) Break as 'internal surf' on distant continental slopes?
3. Develop mixing parameterizations for use in ocean models.
4. Paleo-tides.

Notes by Josefina Arraut and Anja Slim.

References

[1] J. Pedlosky, *Waves in the Ocean and Atmosphere: Introduction to Wave Dynamics* (Springer, New York, 2003).

[2] D. E. Mowbray and B. S. H. Rarity, "A theoretical and experimental investigation of the phase configuration of internal waves of small amplitude in a density stratified fluid," J. Fluid Mech. **28**, 1 (1967).

[3] H. Sandstrom, Ph.D. thesis, University of California at San Diego, 1966.

[4] M. Rattray, J. G. Dworski, and P. E. Kovala, "Generation of long internal waves at the continental slope," Deep-Sea Res. **16 Suppl.**, 179 (1969).

[5] R. Regal and C. Wunsch, "M2 tidal currents in the western North Atlantic," Deep-Sea Res. **20**, 493 (1973).

[6] R. M. Hendry, "Observations of the semidiurnal internal tide in the western North Atlantic Ocean," Phil. Trans. R. Soc. **A286**, 1 (1977).

[7] W. H. Munk, F. E. Snodgrass, and M. Wimbush, "Tides offshore: transition from Califnornia coastal to deep sea waters," Geophys. Fluid Dyn. **1**, 161 (1970).

[8] R. D. Ray and G. T. Mitchum, "Surface manifestation of internal tides in the deep ocean: observations from altimetry and island gauges," Prog. Oceanogr. **40**, 135 (1997).

[9] J. M. Toole, J. R. Ledwell, K. L. Polzin, R. W. Schmitt, E. R. Montgomery, L. St. Laurent, and W. B. Owens, "The Brazil Basin Tracer Release Experiment," International WOCE Newsletter **28**, 25 (1997).

[10] R.-C. Lien and M. C. Gregg, "Observations of turbulence in a tidal beam and across a coastal ridge," J. Geophys. Res. **106**, 4575 (2001).

[11] C. S. Cox and H. Sandstrom, "Coupling of surface and internal waves in water of variable depth," Journal of the Oceanographic Society of Japan, 20th Anniversary Volume 499 (1962).

[12] T. H. Bell, "Topographically generated internal waves in the open ocean," J. Geophys. Res. **80**, 320 (1975).

[13] G. D. Egbert and R. D. Ray, "Significant dissipation of tidal energy in the deep ocean inferred from satellite altimeter data," Nature **405**, 775 (2000).

[14] G. D. Egbert and R. D. Ray, "Estimate of M2 tidal energy dissipation from TOPEX/POSEIDON altimeter data," J. Geophys. Res. **106**, 22475 (2001).

[15] L. St. Laurent and C. Garrett, "The role of internal tides in mixing the deep ocean," J. Phys. Ocean. **32**, 2882 (2002).

[16] S. G. Llewellyn Smith and W. R. Young, "Conversion of the barotropic tide," J. Phys. Ocean. **32**, 1554 (2002).

[17] B. Sjöberg and A. Stigebrandt, "Computations of the geogrpahical distribution of the energy flux to mixing processes via internal tides and the associated vertical circulation in the ocean," Deep-Sea Res. **39**, 269 (1992).

[18] L. St. Laurent, S. Stringer, C. Garrett, and D. Perrault-Joncas, "The generation of internal tides at abrupt topography," Deep-Sea Res. **50**, 987 (2003).

[19] S. G. Llewellyn Smith and W. R. Young, "Tidal conversion at a very steep ridge," J. Fluid Mech **495**, 175 (2003).

[20] N. J. Balmforth, G. R. Ierley, and W. R. Young, "Tidal conversion by nearly critical topography.," J. Phys. Ocean. **32**, 2900 (2002).

[21] F. Pétrélis, S. G. Llewellyn Smith, and W. R. Young, "Tidal conversion at a submarine ridge," J. Phys. Ocean. (2004), *Submitted.*